Journal of Power Sources 340 (2017) 89–97

Contents lists available at ScienceDirect

Journal of Power Sources

journal homepage: www.elsevier.com/locate/jpowsour

In situ characterization of charge rate dependent stress and structure changes in V_2O_5 cathode prepared by atomic layer deposition

Hyun Jung [a, b, c], Konstantinos Gerasopoulos [a, c, 1], A. Alec Talin [d], Reza Ghodssi [a, b, c, *]

[a] MEMS Sensors and Actuators Laboratory (MSAL), University of Maryland, College Park, MD 20742, USA
[b] Department of Electrical and Computer Engineering, University of Maryland, College Park, MD 20742, USA
[c] Institute for Systems Research, University of Maryland, College Park, MD 20742, USA
[d] Sandia National Laboratories, Livermore, CA 94551, USA

HIGHLIGHTS

- Investigated effects of varying C-rates on stress and structure changes in V_2O_5.
- A linear increase in the stress as a function of x in $Li_xV_2O_5$ is observed.
- C-rate does not directly contribute to larger intercalation stress.
- A rapid increase in disorder within $Li_xV_2O_5$ is correlated with higher C-rate.

GRAPHICAL ABSTRACT

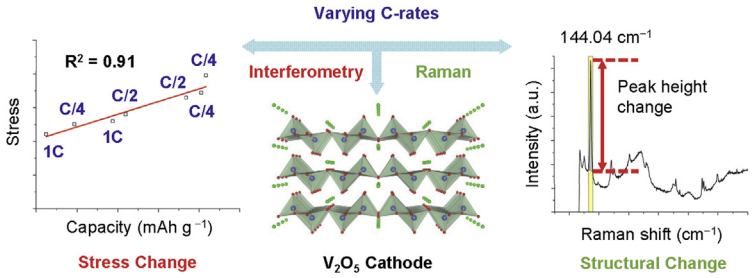

ARTICLE INFO

Article history:
Received 9 August 2016
Received in revised form
8 November 2016
Accepted 10 November 2016

Keywords:
Lithium-ion battery
Vanadium oxide
Charge rates
In situ
Raman spectroscopy
Stress

ABSTRACT

The insertion/extraction of lithium into/from various host materials is the basic process by which lithium-ion batteries reversible store charge. This process is generally accompanied by strain in the host material, inducing stress which can lead to capacity loss. Therefore, understanding of both the structural changes and the associated stress – investigated almost exclusively separate to date – is a critical factor for developing high-performance batteries. Here, we report an *in situ* method, which utilizes Raman spectroscopy in parallel with optical interferometry to study effects of varying charging rates (C-rates) on the structure and stress in a V_2O_5 thin film cathode. Abrupt stress changes at specific crystal phase transitions in the Li–V–O system are observed and the magnitude of the stress changes with the amount of lithium inserted into the electrode are correlated. A linear increase in the stress as a function of x in $Li_xV_2O_5$ is observed, indicating that C-rate does not directly contribute to larger intercalation stress. However, a more rapid increase in disorder within the $Li_xV_2O_5$ layers is correlated with higher C-rate. Ultimately, these experiments demonstrate how the simultaneous stress/Raman *in situ* approach can be utilized as a characterization platform for investigating various critical factors affecting lithium-ion battery performance.

1. Introduction

Lithium-ion batteries (LIBs) provide high energy density while being light-weight and compact, powering a variety of devices such as smartphones, laptops, and desktop computers. New applications

* Corresponding author. MEMS Sensors and Actuators Laboratory (MSAL), Department of Electrical and Computer Engineering, Institute for Systems Research, University of Maryland, College Park, MD 20742, USA.
E-mail address: ghodssi@umd.edu (R. Ghodssi).
[1] Present address: The Johns Hopkins University Applied Physics Laboratory LLC, 11100 Johns Hopkins Road, Laurel, MD 20723, USA.

http://dx.doi.org/10.1016/j.jpowsour.2016.11.035
0378-7753/

such as electric and hybrid vehicles demand even higher energy density, longer cycle life, lower cost, and improved safety [1,2]. Therefore, a considerable amount of research has been directed towards developing new electrode materials. A major challenge in these efforts has been characterizing and understanding these materials while batteries are in a state of operation [3].

Different electrode materials react with Li in a various ways, such as intercalation or alloying [1,4,5]. Irrespective of the exact mechanism, stress generation due to lithiation has been demonstrated to produce cracks or fractures in the host material which result in capacity loss and ultimately failure of the battery. In addition to stress, the host material can experience significant structural and chemical changes such as phase transitions [6–8]. Therefore, measurement techniques which acquire stress and structural evolutions in real time could be useful for understanding mechanisms of LIB degradation and advancing battery performance.

Recently, significant progress has been made with *in situ* techniques based on X-ray diffraction (XRD), scanning transmission X-ray microscopy, and transmission electron microscopy (TEM) in structural characterization of LIB electrodes [9–15]. Compared to the aforementioned techniques which reply on complex electrochemical cells and bulky external equipment, Raman spectroscopy is an alternative method for probing structural changes of LIB electrodes with sub-micron spatial resolution in a relatively simple experimental set up readily compatible with liquid electrolytes and without the need for high vacuum. Raman spectroscopy utilizes inelastic scattering of monochromatic photons by the electrode sample, which can acquire information such as crystallinity/disorder, strain, and chemical composition including Li content [7,16]. *In situ* Raman spectroscopy has been widely applied, from graphite and other carbonaceous materials, to transition metal oxides-based compounds, or solid electrolyte interphase formation [7,17]. Additional insights into the battery operation and degradation mechanisms, as well as identifying which phases are present during abrupt changes in stress, can be achieved by combining *in situ* Raman spectroscopy with stress measurement.

In addition to the characterization of structural changes, significant advances have been made in *in situ* mechanical strain/stress characterization of LIB electrodes using a variety of approaches [18–22]. Among these techniques, the multi-beam optical stress sensor (MOSS) has proven to be an effective method for analyzing the stress evolution in LIB thin film electrodes during battery operation. This technique utilizes a silicon substrate coated with a passivation layer, a current collector, and a thin film active battery material of interest. The stress generated in the active material changes the curvature in the wafer which is measured using an array of parallel laser beams. The curvature change is determined by measuring relative changes in the spacing between the reflected beams, and the resulting stress is calculated using the Stoney equation [20]. While this technique is advantageous for mechanical strain/stress characterization, the experimental setup hinders direct access to the electrode which limits its potential integration with other methods that are capable of characterizing structural evolution in the electrode. Additionally, the stress value calculated using this technique is averaged over the entire wafer-scale. Therefore, the MOSS technique gives the best results when it is applied for materials that experience spatially homogeneous strain/stress.

In this work, we investigate the stress and structural changes in an ALD-deposited thin film $Li_xV_2O_5$ electrode over multiple discharge/charge cycles using an *in situ* characterization platform. Despite large theoretical capacity of ~450 mAh/g, $Li_xV_2O_5$ has not been widely adopted in commercial cells in part due to lower voltage *vs.* Li compared to other Li intercalation oxides such as Li_xCoO_2, and in part due to the complexities of the several phase transitions occurring during Li insertion/extraction reactions and how these relate to battery performance. Previously, C-rate variation has been identified as an important factor affecting battery performance [23–25], and the impact of high C-rate on the structure and associated stress in the electrode have been analyzed. The *in situ* platform utilizes a microelectromechanical systems (MEMS) optical sensor integrated with Raman spectroscopy to enable characterization of both the stress and structural changes in the electrode simultaneously. Our results reveal abnormal stress changes when the $Li_xV_2O_5$ electrode experiences α- to ε-phase and ε- to δ-phase transitions. Additionally, these abnormal stress changes have been observed at higher lithium content in $Li_xV_2O_5$ when the electrode is cycled at higher rates, and the magnitude of the stress changes have been correlated with the amount of lithium inserted into the electrode. Moreover, we find signs of a more uniform lithium concentration throughout the electrode with decreasing electrode thickness at the same C-rate. We are also able to analyze Raman peak intensity changes of the translational mode at low frequency (144 cm^{-1}) as a function of x in $Li_xV_2O_5$, showing a faster increase of disorder within the $Li_xV_2O_5$ layers when the electrode is cycled at higher C-rates.

2. Methods and experimental

The MEMS optical sensor (Fig. 1a) used in this work is composed of an array of flexible circular membranes. These membranes divide the sensor into two cavities, referred to as the 'optical' and 'battery' cavities. The optical cavity is formed by anodically bonding glass to a silicon wafer. The battery cavity, which is much deeper, is formed on the other side of the membrane (Si_3N_4, 700 nm) coated with an insulating layer (SiO_2, 250 nm), a current collector (Cr/Au, 15/10 nm), and an active battery material (V_2O_5, 200 nm). The battery cavity simultaneously provides a channel for the liquid electrolyte. The detailed sensor fabrication procedure is described in our previous work [21].

The V_2O_5 thin films are deposited in a BENEQ TFS 500 atomic layer deposition (ALD) reactor by alternating pulses of vanadium triisopropoxide (VTOP) and ozone at 170 °C. The V_2O_5 deposition rate is measured as 0.81 Å/cycle. The V_2O_5 was deposited for 2470 cycles toward a target thickness of 200 nm. The mass of the active material is measured with a high precision microbalance (Mettler Toledo, XS105 dualRange, 1 μg) before and after the deposition.

Packaging for the sensor is achieved using a modified coin cell with an optical window. First, the optical window (5 mm in diameter) is machined into the coin cell cap (LIR2032), and double-sided adhesive aluminum tape (1170 tape, 3M) is placed between the cap and the sensor. A hermetic seal and electron transport are achieved by adhesive aluminum tape. The active material deposited on the sensor and metallic lithium (Sigma Aldrich) pressed against a stainless steel disc serve as the cathode and anode, respectively. A polymer separator (Celgard® 3501) is placed between the two electrodes and soaked with liquid electrolyte (1 M $LiPF_6$ solution in ethyl carbonate/dimethyl carbonate (EC/DMC, 1:1 by volume), Novolyte Technologies). The cell is closed in an argon filled glove box with oxygen concentration of less than 0.1 ppm.

The assembled coin cell is connected to a potentiostat (Compactstat, Ivium Technologies) and placed under a Raman microscope for galvanostatic testing (Fig. 2). This *in situ* experimental setup utilizes a Raman microscope (Yvon Jobin LabRam ARAMIS, Horiba, Ltd.) where the white-light illumination source is replaced with a despeckled 532 nm green laser (CPS532, Thorlab Inc.) for monitoring the membrane deflection using optical interferometry (Fig. 2, interferometric laser). The same microscope is used for monitoring the structure changes of the electrode using a 532 nm

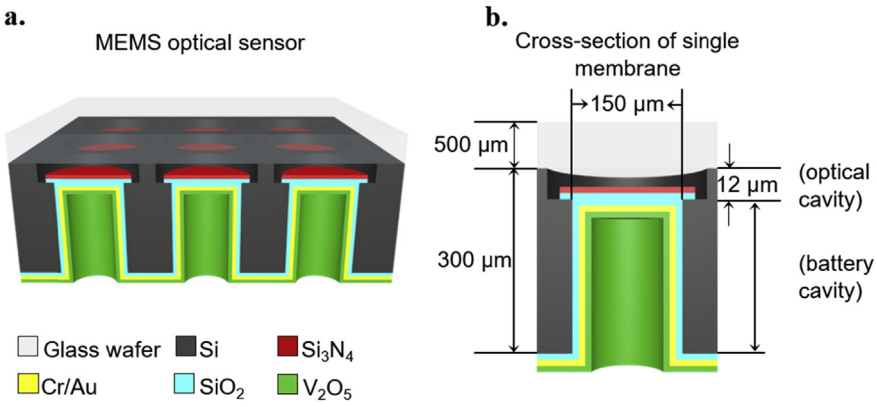

Fig. 1. MEMS optical sensor geometry. (a) 3D schematic of MEMS optical sensor showing array of circular membranes. (b) Cross-section diagrams of a single membrane; shallow optical cavity at the top and deep battery cavity below.

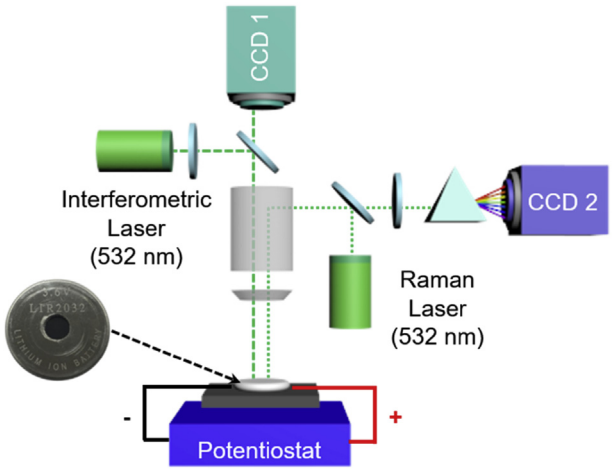

Fig. 2. Simplified schematic diagrams of the Raman microscope experimental setup showing the location of the coin cell under test relative to the Raman microscope.

Nd:YAG laser as the excitation source (Fig. 2, Raman laser) for Raman spectroscopy measurements. A 10× objective is used to focus the Raman laser onto the electrode surface (spot size ~6.76 μm^2) and the Raman spectra are collected in a back-scattering configuration. The power of the laser beam is adjusted using a neutral density filter to avoid local heating of the electrode. Each spectrum is collected for 90 s in total with three 30 s accumulations. An interference pattern is produced when the interferometric laser illuminates one of the membranes in the optical cavity of the sensor (Fig. 4). The as-fabricated sensor membranes have some residual stress associated with the fabrication processes which result in an upward curvature [21]. Due to this pre-deflected circular membrane, the initial interference pattern already shows multiple concentric rings. The Raman laser is used to probe the V_2O_5 electrode underneath the glass wafer and the multi-layer membrane (Supplementary Fig. 1). The imaging software (NGSLapSpec, Horiba, Ltd.) supports user specific operations programmed in Visual Basic Script. This enables automatic switching between the two laser sources repeatedly throughout the experiment to collect the corresponding data. Electrochemical experiments are performed in the half-cell configuration in ambient conditions. Galvanostatic lithium cycling experiment is conducted from 2.80 to 3.75 V at different C-rates: C/4, C/2, and 1C.

An estimation of the stress change in the $Li_xV_2O_5$ electrode can be made under the assumption that changes in Young's modulus and thickness of the $Li_xV_2O_5$ electrode during the lithium insertion/extraction process are negligible. In this case, a differential stress change in $Li_xV_2O_5$ can be estimated using analytical calculations. Since the thickness of the flexible membrane of the MEMS optical sensor is 1.18 μm and the membrane deflects the same order of magnitude, the membrane behavior should follow a thick circular clamped membrane described by Equation (1) [26],

$$p = 4\frac{dw_0}{R_v^2}\left(\frac{4}{3}\frac{d^2}{R_v^2}\frac{E}{1-\nu^2} + \sigma_0 + \frac{64}{105}\frac{w_0^2}{R_v^2}\frac{E}{1-\nu^2}\right) \quad (1)$$

where p is the differential pressure acting on the membrane, d is thickness of the membrane, w_0 is the initial membrane deflection, R_v is radius of the membrane, E is Young's modulus of the membrane, v is Poisson's ratio of the membrane, and σ_0 is initial stress in the membrane.

As shown in Fig. 4a, at the beginning of our experiment, the interference pattern of the pristine electrode is composed of 11 concentric rings. Each of the concentric rings is generated when the membrane deflection is equal to half of the wavelength of the light source. Since the wavelength of the light source is 532 nm, the initial membrane deflection (w_0) is 2.93 μm. Therefore, the differential pressure (p) can be determined from Equation (1). The parameters used in this calculation are specified in Table 1.

During the lithium insertion process, the membrane receives tensile stress and the membrane deflection becomes smaller. As a result, the intensity at the center of the membrane changes from bright (Fig. 4a) to dark (Fig. 4b), which is equal to 133 nm (λ/4) deflection of the membrane. Therefore, the membrane deflection of the electrode under testing (Fig. 4b) becomes 2.80 μm (w_1). However, the differential pressure does not change during the electrochemical discharge-charge process. The only factor inducing the smaller deflection of the membrane is the stress change in the membrane (σ_1). By utilizing the differential pressure value achieved

Table 1
Parameters used for the stress estimation presented in this study.

Parameter	Value	Comments
Differential pressure (p)	1.77 MPa	Calculated
Thickness of the membrane (d)	1.18 μm	Measured
Initial membrane deflection (w_o)	2.93 μm	Measured
Radius of the membrane (R_v)	75 μm	Measured
Young's modulus of the membrane (E)	215.65 GPa	[27–29]
Poisson's ratio of the membrane (v)	0.25	[27–29]
Initial membrane stress (σ_0)	451.52 MPa	[30]

in the previous step, the change of the stress in the membrane can be back calculated from Equation (2). According to our calculations, the differential stress change in the $Li_xV_2O_5$ electrode is equal to 303 MPa.

$$p = 4\frac{dw_1}{R_v^2}\left(\frac{4}{3}\frac{d^2}{R_v^2}\frac{E}{1-\nu^2} + \sigma_1 + \frac{64}{105}\frac{w_1^2}{R_v^2}\frac{E}{1-\nu^2}\right) \quad (2)$$

3. Results and discussion

In order to investigate effects of different C-rates on the stress and structural changes in the V_2O_5 cathode, we apply varying C-rates and monitor their impacts on the electrode. Fig. 3 shows galvanostatic discharge-charge curve of the ALD-deposited V_2O_5 thin film electrode upon cycling at different C-rates: C/4, C/2, 1C, and C/4. At each rate, the battery is tested for 2 cycles to minimize the impacts from previous cycles with different C-rates. The discharge-charge curve shows the α- to ε-phase and ε- to δ-phase transformation plateaus at 3.4 and 3.2 V, respectively. The observed electrochemical behavior corresponds to well-known phase transitions previously reported [31,32]. This result demonstrates that the customized cell functions properly in ambient conditions.

To analyze the stress changes in the $Li_xV_2O_5$ electrode during lithium cycling, the interference patterns from the sensor membrane are recorded throughout the experiment. As the stress in the electrode changes during the discharge-charge processes, the flexible membrane deflects causing the intensity of the interference pattern to change. First, the interference pattern of the pristine electrode (Fig. 4a, before the initial discharge process) is recorded and then compared to the interference patterns of the electrode under testing (Fig. 4b). Specifically, the intensity changes at the center of the membrane are analyzed since it is the part of the membrane most sensitive to changes in stress. In order to verify how the intensity varies with stress in the membrane, the change of interference intensity as a function of membrane stress is simulated using MATLAB (Supplementary Fig. 2). The details of the analytical

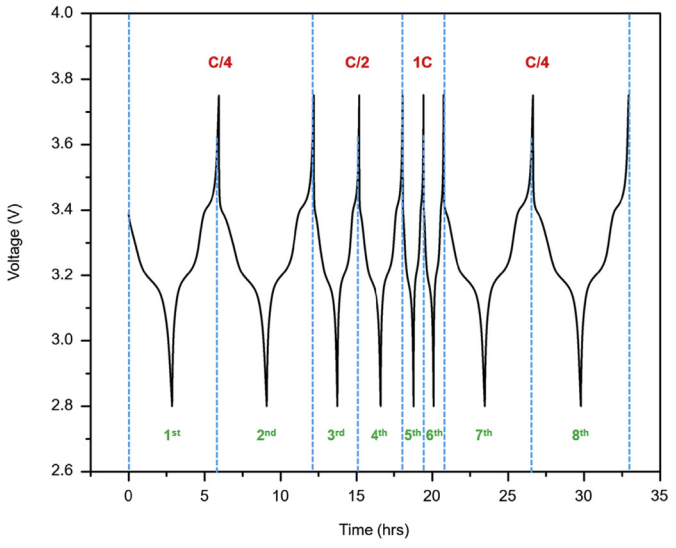

Fig. 3. Galvanosatic discharge-charge cycling curve of the ALD-deposited V_2O_5 electrode achieved from the *in situ* experimental setup. Different C-rates (C/4, C/2, and 1C in red) are applied for different cycles (blue); corresponding cycle numbers are indicated in green in the potential window of 2.8–3.75 V. (For interpretation of the references to colour in this figure legend, the reader is referred to the web version of this article.)

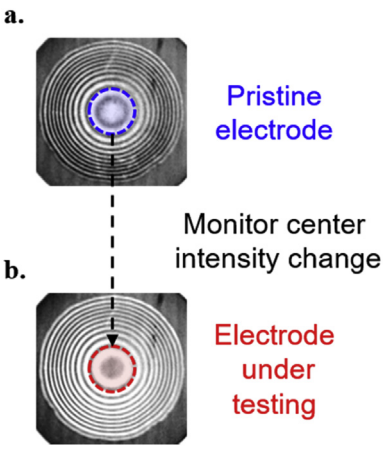

Fig. 4. (a) Interference patterns of the pristine electrode and (b) electrode under testing. Intensity change at the center of the membrane is highlighted within the dotted circles.

equations used in the simulation can be found in our previous work [21], and the parameters used in this simulation are specified in Supplementary Table 1. According to our simulation, a first-order linear correlation between the intensity and stress provides an excellent approximation ($R^2 = 0.99$). Therefore, a decrease in the interference intensity directly corresponds to increasing tensile stress in the membrane, with an increase in the intensity conversely corresponding to increasing compressive stress. This intensity change has been correlated with the stress change in the $Li_xV_2O_5$ electrode using the analytical calculations described in the methods and experimental section.

Fig. 5 displays superposition of the discharge-charge curves over the stress changes at different C-rates. Correlation between the stress and electrochemical discharge-charge of the second cycle (Fig. 3, C/4) is shown in Fig. 5a. Upon lithium intercalation, the stress in the electrode becomes increasingly tensile in general (Fig. 5a, blue dotted arrow from 90 to 210 MPa). This result is in agreement with previously published XRD studies [31,33]. During the lithium intercalation process, $Li_xV_2O_5$ changes from α- to δ-phase and the phase transition is accompanied by evolutions in the *a* and *b* lattice parameters. XRD measurements have shown that the *a* lattice parameter continuously decreases while the *b* parameter remains relatively constant during the phase transition. Since the ALD-deposited V_2O_5 has a preferential growth in (001) orientation (Supplementary Fig. 3), changes in the *c* lattice parameter should not affect the stress in the membrane which is free to expand. Therefore, these lattice parameter changes should only increase the tensile stress. However, abnormal stress changes (inflections) are observed, indicated by the red dotted lines in Fig. 5a, and these inflections coincide with well-known two-phase transitions (α- to ε-phase and ε- to δ-phase) during lithiation of V_2O_5 [7,31,32]. These inflections are abnormal since the $Li_xV_2O_5$ experiences increases in compressive stress despite the fact that the lattice parameter *a* continuously decreases. This observation indicates that the coexistence of two distinct phases of $Li_xV_2O_5$ is responsible for the abnormal stress changes in the electrode, which has not been previously reported in the XRD studies. These inflections are analyzed in more detail to investigate the effect of higher C-rates on the $Li_xV_2O_5$ electrode. Upon lithium extraction, the stress returns to its initial value.

Analysis on the stress change and electrochemical discharge-charge of the fourth cycle (Fig. 3, C/2) is shown in Fig. 5b. Upon discharge, similar stress change is observed, with the same inflections as seen in the second cycle (Fig. 5a). However, the

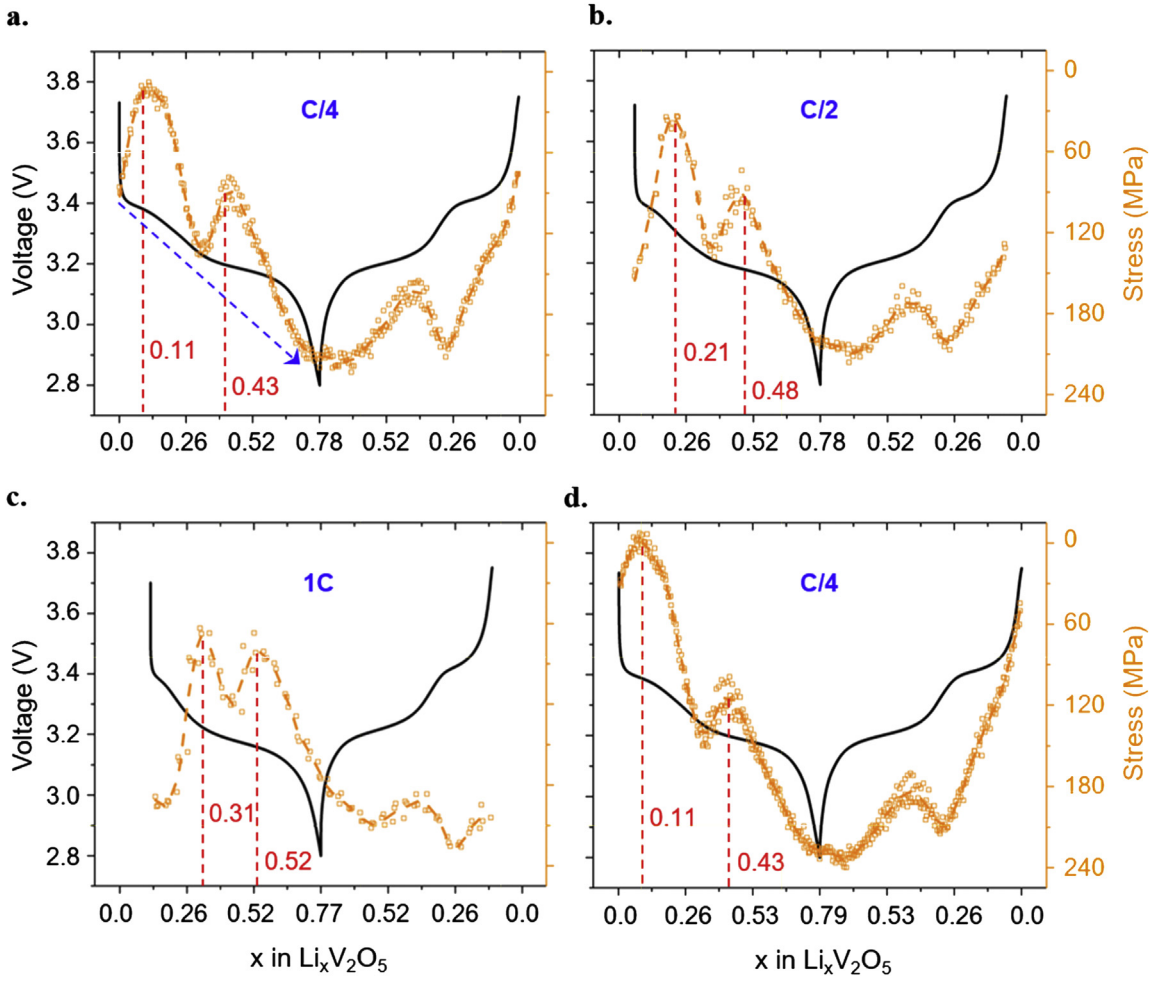

Fig. 5. Correlation between stress changes and potential variations during discharge-charge processes of the (a) second (C/4), (b) fourth (C/2), (c) sixth (1C), and (d) eighth (C/4) cycles. Abnormal stress changes observed during discharge processes are marked in red dotted lines. Different C-rates are marked in blue. (For interpretation of the references to colour in this figure legend, the reader is referred to the web version of this article.)

inflections in the stress change emerge when the amount of lithium in $Li_xV_2O_5$ is greater (when x = 0.21 and 0.48) than in the second cycle (when x = 0.11 and 0.43). The same phenomenon is also observed in the sixth cycle (Fig. 5c), and the inflections are observed when the amount of lithium in $Li_xV_2O_5$ is further increased (when x = 0.31 and 0.52). This behavior is believed to be the result of the low diffusion coefficient of lithium ions (10^{-12}–10^{-13} cm^2 s^{-1}) in V_2O_5 electrodes [34–37], which has also been reported by Soni et al. for thin film Si electrodes [38]. We surmise that at higher C-rates (C/2 and C) the increased Li concentration at the $Li_xV_2O_5$/electrolyte interface results in a steeper [Li] gradient across the $Li_xV_2O_5$ film and inhomogeneous α- to ε-phase and ε- to δ-phase transitions. This diffusion limited insertion of lithium in the $Li_xV_2O_5$ electrode also explains the decreasing discharge capacity (115.53 to 96.40 mAh g^{-1}) when cycled at higher C-rates (Fig. 6, C/4 to 1C). When the $Li_xV_2O_5$ electrode is cycled at the lowest C-rate again (Fig. 5d, C/4), lithium concentration gradient across the $Li_xV_2O_5$ film becomes more uniform and as a result, the inflections are observed at the lower lithium concentrations again (when x = 0.11 and 0.43).

It has been previously reported that when the battery is charged at a rate faster than lithium can homogenize in an active particle by diffusion, the inhomogeneous distribution of lithium results in high stresses that may cause the particle to fracture [39]. Also, it has

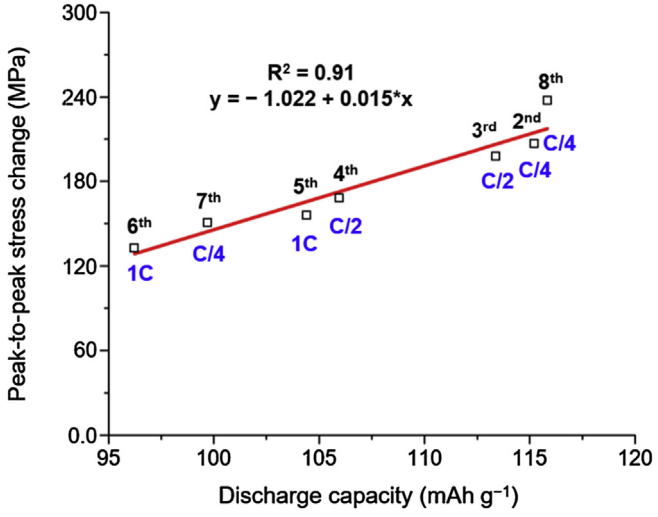

Fig. 6. Correlation between the peak-to-peak stress change and discharge capacity variation at different cycles. Cycle numbers are specified in black and their corresponding C-rates in blue. (For interpretation of the references to colour in this figure legend, the reader is referred to the web version of this article.)

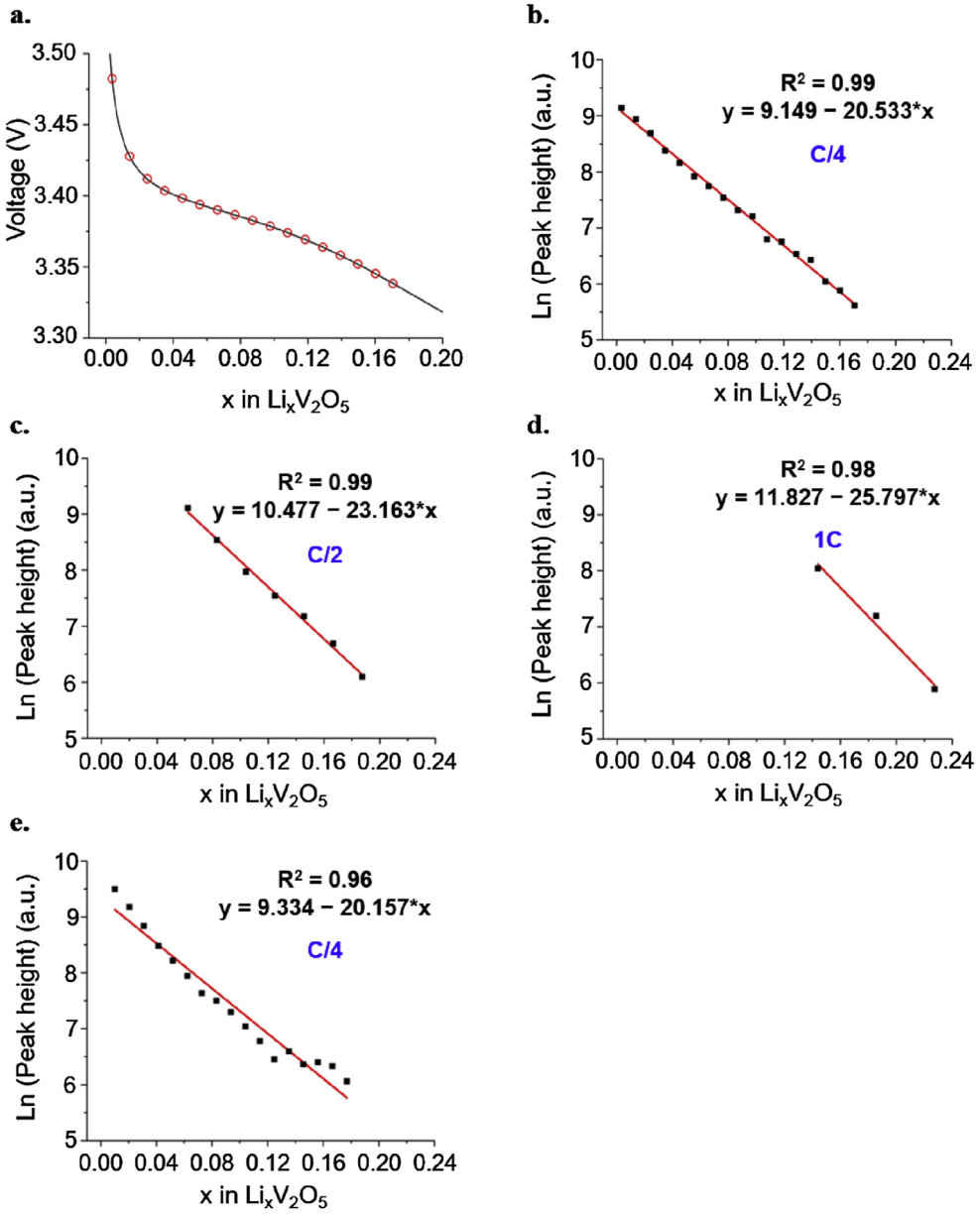

Fig. 7. (a) Discharge curve of the second cycle; red circles correspond to the point where the *in situ* Raman spectra are analyzed. Correlation between the natural log of the peak height at the 144 cm^{-1} mode as a function of the lithium insertion in $Li_xV_2O_5$ electrode when discharged at (b) C/4 (2nd cycle), (c) C/2 (4th cycle), (d) 1C (6th cycle), and (e) C/4 (8th cycle). Different C-rates are marked in blue. (For interpretation of the references to colour in this figure legend, the reader is referred to the web version of this article.)

been simulated that spherical particles experience larger intercalation-induced stresses when discharged under larger current densities [40]. Therefore, our experiments have been focusing on analyzing C-rate dependent stress change in a thin film electrode in order to verify whether the higher C-rate induces increased stress in the electrode. Fig. 6 displays correlation between the peak-to-peak magnitude of the change in stress and the discharge capacity measured at different C-rates. Based on our findings, the observed linear dependence ($R^2 = 0.91$) indicates that the magnitude of the stress change in the thin film $Li_xV_2O_5$ electrode is determined by the total amount of lithium intercalated into the electrode rather than how fast/slowly it is discharged.

Concomitant with monitoring the stress, a series of *in situ* Raman spectra of the $Li_xV_2O_5$ electrode are measured throughout the experiment. The optical cavity of the sensor (Fig. 1b) enables the Raman excitation source to probe the structural changes in the $Li_xV_2O_5$ electrode. The Raman spectrum of the as-deposited V_2O_5 thin film displays nine peaks from 100 to 1000 cm^{-1}, located at 144, 196, 283, 303, 403, 482, 527, 701, and 995 cm^{-1} (Supplementary Fig. 1), in agreement with previously reported Raman spectra [41]. This result verifies that the Raman excitation laser source penetrates the transparent glass wafer and the thin multi-layer membrane to probe the V_2O_5 electrode underneath.

Previously, structural disorder of $Li_xV_2O_5$ due to lithiation has been correlated with decreasing in intensity of the 144 cm^{-1} Raman line (mixture of B_{1g} and B_{3g} modes) [7,42]. Therefore, changes in the intensity (peak height) of the 144 cm^{-1} mode during lithium insertion (discharge) have been characterized (Supplementary Fig. 4) to investigate how the level of disorder in the $Li_xV_2O_5$ electrode changes when it is cycled at different C-rates. First, *in situ* Raman spectra are measured during the second cycle discharge process (Fig. 7a) and their corresponding peak heights at

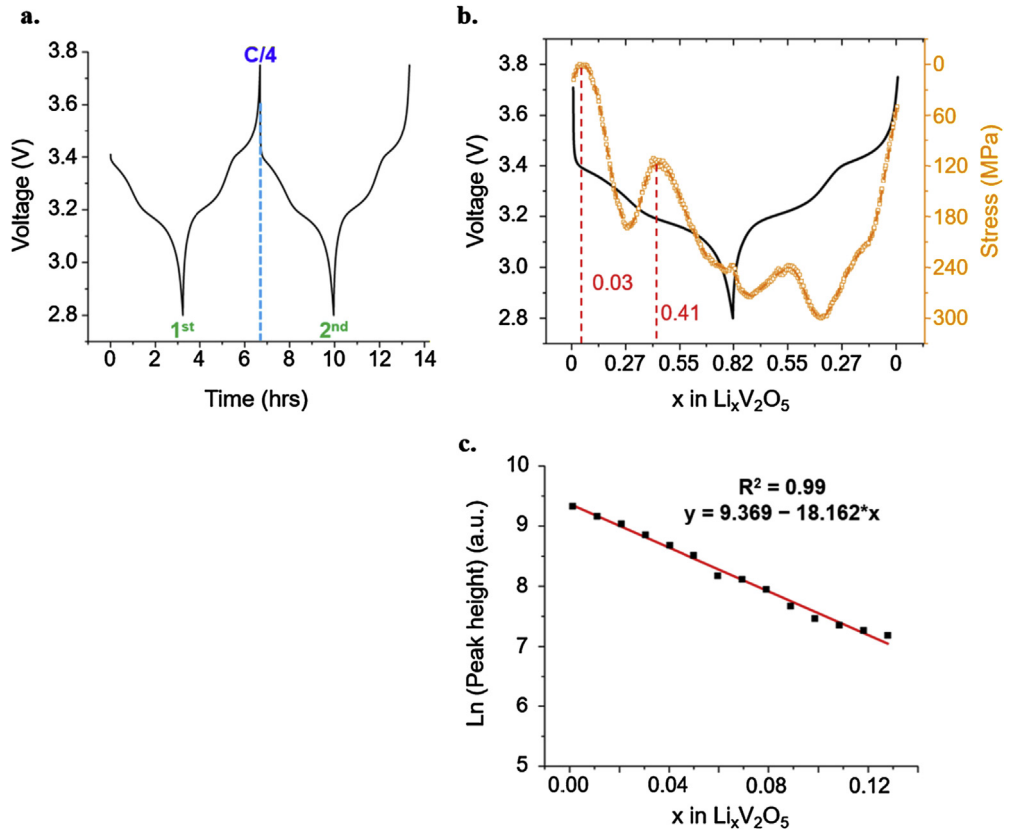

Fig. 8. (a) Galvanosatic discharge-charge cycling curve of the ALD-deposited V_2O_5 electrode (150 nm) cycled at C/4 throughout the experiment; corresponding cycle numbers are indicated in green in the potential window of 2.8–3.75 V. (b) Correlation between stress change and potential variation during discharge-charge processes of the second cycle. (c) Correlation between the natural log of the peak height at the 144 cm^{-1} mode as a function of the lithium insertion in $Li_xV_2O_5$ electrode (150 nm) during the second cycle discharge process. (For interpretation of the references to colour in this figure legend, the reader is referred to the web version of this article.)

the 144 cm^{-1} mode are correlated with Li concentration in the $Li_xV_2O_5$ electrode (Fig. 7b). The exponential dependence of the 144 cm^{-1} peak intensity on the degree of lithiation in $Li_xV_2O_5$ electrode has not been previously observed. We next use this dependence to investigate the impact of C-rate on the structure of the $Li_xV_2O_5$.

When the $Li_xV_2O_5$ electrode is discharged at higher C-rates (C/2, and 1C), the 144 cm^{-1} peak height also decreases exponentially as a function of the amount of lithium in the electrode (Fig. 7c and d). However, the slope of the fitted lines changed from −20.53 to −25.80 (Fig. 7b–d) as the C-rates are increased from C/4 to 1C. This indicates that the disorder in the $Li_xV_2O_5$ electrode increases faster when it is discharged at higher C-rates, even when the same amount of lithium is inserted into the electrode. This shows that the level of disorder in the electrode depends on both the lithiation level and the C-rate. When the C-rate is decreased to C/4 again, the slope of the fitted line increased back to −20.16 (Fig. 7e) which is almost identical to the value obtained in Fig. 7b. We believe the recovery of the slope from −25.80 (1C) to −20.16 (C/4) corresponds to the reversible structural changes in the $Li_xV_2O_5$ electrode within the voltage range from 3.75 to 2.8 V [42].

After studying the C-rate dependent stress and structural changes in the $Li_xV_2O_5$ electrode, we extend our focus into thickness of the electrode since it is also an important factor that can affect the battery performance. Previously, Soni et al. [38,43] reported thickness effects on the lithiation of amorphous Si thin films to study effects of the electrode thickness on battery performance. According to their work, a characteristic time $\tau \sim h_0^2/D_{Li}$ is defined [43] that provides a useful interpretation of their results, where h_0 is the initial electrode thickness and D_{Li} is the diffusion coefficient of lithium ions. When τ is small, the Li concentration gradient through the film is nearly uniform. On the other hand, larger values of τ lead to significant concentration gradients. Therefore, we would expect the thinner electrode to result in a more uniform Li concentration gradient compared to the thicker film when both electrodes are cycled at the same C-rate.

In order to further investigate the effects of film thickness on the stress and structural changes, a thinner V_2O_5 electrode (150 nm) has been prepared and characterized at the lowest C-rate (Fig. 8a). The thinner V_2O_5 thin films are deposited using the same ALD reactor (BENEQ TFS 500) by alternating pulses of vanadium triisopropoxide (VTOP) and ozone at 170 °C for 1852 cycles. Fig. 8b displays superposition of the discharge-charge curve over the stress change at C/4 during the second discharge-charge process. The stress change shows the same trend which is shown in Fig. 5a. However, the abnormal stress changes are observed when the amount of lithium in $Li_xV_2O_5$ is further decreased (when x = 0.03 and 0.41) compared to the thicker (200 nm) V_2O_5 electrode at C/4 (Fig. 5a, when x = 0.11 and 0.43). This result indicates that the thinner electrode will exhibit greater uniformity in the Li concentration gradient throughout the electrode.

In terms of the structure change, the exponential dependence of the 144 cm^{-1} peak intensity on the degree of lithiation in $Li_xV_2O_5$ electrode has been characterized for the second cycle (Fig. 8a) and the results are shown in Fig. 8c. The slope of the fitted line increased to −18.162 compared to the −20.533 and −20.157 which are the slopes of the fitted lines for the thicker V_2O_5 electrode cycled at C/4 (Fig. 7b, e). These results show that the thinner $Li_xV_2O_5$ electrode

responds as if the electrode is cycled at lower C-rates, resulting in higher uniformity in Li concentration gradient throughout the electrode.

4. Conclusions

By taking full advantage of the MEMS optical sensor integrated with *in situ* Raman spectroscopy, the effects of lithiation level and increasing C-rates on the stress and structural evolutions in ALD-deposited $Li_xV_2O_5$ electrode have been successfully characterized. We have shown that the magnitude of the stress changes in the $Li_xV_2O_5$ electrode increase linearly with the amount of lithium present in the electrode, indicating increasing C-rate does not directly induce larger stresses in the $Li_xV_2O_5$ thin film electrode. At the same time, inflections in the stress evolution, which are observed when the $Li_xV_2O_5$ electrode is experiencing α- to ε-phase and ε- to δ-phase transitions, required a greater amount of lithium as the electrode is cycled at higher C-rates. We believe this behavior is caused by the slow lithium-ion diffusion in the $Li_xV_2O_5$ lattice, causing steeper lithium concentration gradients through the $Li_xV_2O_5$ film thickness when it is cycled at higher C-rates. Raman spectra collected *in operando* have demonstrated an exponential dependence of the 144 cm^{-1} mode on Li concentration in $Li_xV_2O_5$ and that this peak decreases faster when cycled at higher C-rates. At C/4-rate, the variation in the 144 cm^{-1} peak intensity reverts to its original trend, suggesting that the structural changes in the $Li_xV_2O_5$ electrode observed at higher C-rates are reversible. Additionally, we have demonstrated that the thinner $Li_xV_2O_5$ electrode results in higher uniformity in Li concentration gradient throughout the electrode compared to the thicker $Li_xV_2O_5$ electrode when cycled at the same C-rate.

Acknowledgements

This work was supported as part of the Nanostructures for Electrical Energy Storage (NEES), an Energy Frontier Research Center funded by the U.S. Department of Energy, Office of Science, Basic Energy Sciences under Award number DESC0001160. The authors acknowledge the staff at Maryland Nanocenter, AIMLab, and Surface Analysis Center. Sandia National Laboratories is a multi-program laboratory managed and operated by Sandia Corporation, a wholly owned subsidiary of Lockheed Martin Corporation, for the U.S. Department of Energy's National Nuclear Security Administration under contract DE-AC04-94AL85000.

Appendix A. Supplementary data

Supplementary data related to this article can be found at http://dx.doi.org/10.1016/j.jpowsour.2016.11.035.

References

[1] N. Nitta, F. Wu, J.T. Lee, G. Yushin, Li-ion battery materials: present and future, Mater. Today 18 (2015) 252–264, http://dx.doi.org/10.1016/j.mattod.2014.10.040.
[2] J.-J. Woo, Z. Zhang, K. Amine, Separator/electrode assembly based on thermally stable polymer for safe lithium-ion batteries, Adv. Energy Mater. 4 (2014), http://dx.doi.org/10.1002/aenm.201301208 n/a-n/a.
[3] P.P.R.M.L. Harks, F.M. Mulder, P.H.L. Notten, *In situ* methods for Li-ion battery research: a review of recent developments, J. Power Sources 288 (2015) 92–105, http://dx.doi.org/10.1016/j.jpowsour.2015.04.084.
[4] J.-M. Tarascon, M. Armand, Issues and challenges facing rechargeable lithium batteries, Nature 414 (2001) 359–367, http://dx.doi.org/10.1038/35104644.
[5] C.M. Hayner, X. Zhao, H.H. Kung, Materials for rechargeable lithium-ion batteries, Annu. Rev. Chem. Biomol. Eng. 3 (2012) 445–471, http://dx.doi.org/10.1146/annurev-chembioeng-062011-081024.
[6] D. Qian, C. Ma, K.L. More, Y.S. Meng, M. Chi, Advanced analytical electron microscopy for lithium-ion batteries, NPG Asia Mater. 7 (2015) e193, http://dx.doi.org/10.1038/am.2015.50.
[7] R. Baddour-Hadjean, J.-P. Pereira-Ramos, Raman microspectrometry applied to the study of electrode materials for lithium batteries, Chem. Rev. 110 (2010) 1278–1319, http://dx.doi.org/10.1021/cr800344k.
[8] M. Winter, J.O. Besenhard, M.E. Spahr, P. Novák, Insertion electrode materials for rechargeable lithium batteries, Adv. Mater. 10 (1998) 725–763, http://dx.doi.org/10.1002/(SICI)1521-4095(199807)10:10<725::AID-ADMA725>3.0.CO;2-Z.
[9] E.S. Takeuchi, A.C. Marschilok, K.J. Takeuchi, A. Ignatov, Z. Zhong, M. Croft, Energy dispersive X-ray diffraction of lithium-silver vanadium phosphorous oxide cells: *in situ* cathode depth profiling of an electrochemical reduction-displacement reaction, Energy Environ. Sci. 6 (2013) 1465–1470, http://dx.doi.org/10.1039/C3EE40152A.
[10] G.G. Amatucci, J.M. Tarascon, L.C. Klein, CoO_2, the end member of the Li_xCoO_2 solid solution, J. Electrochem. Soc. 143 (1996) 1114–1123, http://dx.doi.org/10.1149/1.1836594.
[11] J. Wang, Y.K. Chen-Wiegart, J. Wang, *In operando* tracking phase transformation evolution of lithium iron phosphate with hard X-ray microscopy, Nat. Commun. 5 (2014), http://dx.doi.org/10.1038/ncomms5570.
[12] M. Ebner, F. Marone, M. Stampanoni, V. Wood, Visualization and quantification of electrochemical and mechanical degradation in Li ion batteries, Science 342 (2013) 716–720. http://science.sciencemag.org/content/342/6159/716.abstract.
[13] D.J. Miller, C. Proff, J.G. Wen, D.P. Abraham, J. Bareño, Observation of microstructural evolution in Li battery cathode oxide particles by *in situ* electron microscopy, Adv. Energy Mater. 3 (2013) 1098–1103, http://dx.doi.org/10.1002/aenm.201300015.
[14] Y.-M. Chiang, Building a better battery, Science 330 (2010) 1485–1486. http://science.sciencemag.org/content/330/6010/1485.abstract.
[15] C.-F. Sun, K. Karki, Z. Jia, H. Liao, Y. Zhang, T. Li, et al., A beaded-string silicon anode, ACS Nano 7 (2013) 2717–2724, http://dx.doi.org/10.1021/nn4001512.
[16] D.V. Esposito, J.B. Baxter, J. John, N. Lewis, T.P. Moffat, T. Ogitsu, et al., Methods of photoelectrode characterization with high spatial and temporal resolution, Energy Environ. Sci. 8 (2015) 2863–2885, http://dx.doi.org/10.1039/C5EE00835B.
[17] V. Stancovski, S. Badilescu, In situ Raman spectroscopic-electrochemical studies of lithium-ion battery materials: a historical overview, J. Appl. Electrochem. 44 (2014) 23–43, http://dx.doi.org/10.1007/s10800-013-0628-0.
[18] K.Y. Chung, K.-B. Kim, Investigation of structural fatigue in spinel electrodes using *in situ* laser probe beam deflection technique, J. Electrochem. Soc. 149 (2002) A79–A85, http://dx.doi.org/10.1149/1.1426396.
[19] H. Mukaibo, T. Momma, Y. Shacham-Diamand, T. Osaka, M. Kodaira, *In situ* stress transition observations of electrodeposited Sn-based anode materials for lithium-ion secondary batteries, Electrochem. Solid State Lett. 10 (2007) A70, http://dx.doi.org/10.1149/1.2426410.
[20] V.A. Sethuraman, V. Srinivasan, A.F. Bower, P.R. Guduru, *In situ* measurements of stress-potential coupling in lithiated silicon, J. Electrochem. Soc. 157 (2010) A1253–A1261, http://dx.doi.org/10.1149/1.3489378.
[21] E. Pomerantseva, H. Jung, M. Gnerlich, S. Baron, K. Gerasopoulos, R. Ghodssi, A MEMS platform for *in situ*, real-time monitoring of electrochemically induced mechanical changes in lithium-ion battery electrodes, J. Micromec. Microeng. 23 (2013) 114018, http://dx.doi.org/10.1088/0960-1317/23/11/114018.
[22] M. Pharr, Z. Suo, J.J. Vlassak, Measurements of the fracture energy of lithiated silicon electrodes of Li-ion batteries, Nano Lett. 13 (2013) 5570–5577, http://dx.doi.org/10.1021/nl403197m.
[23] U. Boesenberg, M. Falk, C.G. Ryan, R. Kirkham, M. Menzel, J. Janek, et al., Correlation between chemical and morphological heterogeneities in $LiNi_{0.5}Mn_{1.5}O_4$ spinel composite electrodes for lithium-ion batteries determined by micro-X-ray, Chem. Mater. (2015), http://dx.doi.org/10.1021/acs.chemmater.5b00119, 150319080353008.
[24] J. Li, N.J. Dudney, X. Xiao, Y.T. Cheng, C. Liang, M.W. Verbrugge, Asymmetric rate behavior of Si anodes for lithium-ion batteries: ultrafast de-lithiation versus sluggish lithiation at high current densities, Adv. Energy Mater. 5 (2015) 1–6, http://dx.doi.org/10.1002/aenm.201401627.
[25] G. Ning, B. Haran, B.N. Popov, Capacity fade study of lithium-ion batteries cycled at high discharge rates, J. Power Sources 117 (2003) 160–169, http://dx.doi.org/10.1016/S0378-7753(03)00029-6.
[26] W.K. Schomburg, C. Goll, Design optimization of bistable microdiaphragm valves, Sens. Actuators A Phys. 64 (1998) 259–264, http://dx.doi.org/10.1016/S0924-4247(97)01612-9.
[27] D.W. Su, S.X. Dou, G.X. Wang, Hierarchical orthorhombic V_2O_5 hollow nanospheres as high performance cathode materials for sodium-ion batteries, J. Mater. Chem. A 2 (2014) 11185–11194, http://dx.doi.org/10.1039/C4TA01751J.
[28] O. Tabata, K. Kawahata, S. Sugiyama, I. Igarashi, Mechanical property measurements of thin films using load-deflection of composite rectangular membranes, Sens. Actuators 20 (1989) 135–141, http://dx.doi.org/10.1016/0250-6874(89)87111-2.
[29] W.N. Sharpe, J. Pulskamp, D.S. Gianola, C. Eberl, R.G. Polcawich, R.J. Thompson, Strain measurements of silicon dioxide microspecimens by digital imaging processing, Exp. Mech. 47 (2007) 649–658, http://dx.doi.org/10.1007/s11340-006-9010-z.
[30] J. Laconte, D. Flandre, J.-P. Raskin, Micromachined Thin-Film Sensors for SOI-CMOS Co-Integration, Springer, US, 2006, http://dx.doi.org/10.1007/0-387-28843-0.

[31] C. Delmas, H. Cognacauradou, J. Cocciantelli, M. Menetrier, J. Doumerc, The $Li_xV_2O_5$ system: an overview of the structure modifications induced by the lithium intercalation, Solid State Ion. 69 (1994) 257–264, http://dx.doi.org/10.1016/0167-2738(94)90414-6.
[32] J.M. Cocciantelli, J.P. Doumerc, M. Pouchard, M. Broussely, J. Labat, Crystal chemistry of electrochemically inserted $Li_xV_2O_5$, J. Power Sources 34 (1991) 103–111, http://dx.doi.org/10.1016/0378-7753(91)85029-V.
[33] E. Meulenkamp, In-situ X-ray diffraction of Li intercalation in sol–gel V_2O_5 films, Solid State Ion. 126 (1999) 235–244, http://dx.doi.org/10.1016/S0167-2738(99)00243-X.
[34] Y. Wang, K. Takahashi, K. Lee, G. Cao, Nanostructured vanadium oxide electrodes for enhanced lithium-ion intercalation, Adv. Funct. Mater. 16 (2006) 1133–1144, http://dx.doi.org/10.1002/adfm.200500662.
[35] D.-Y. Yoo, I.-H. Yeo, W. Il Cho, Y. Kang, S.-I. Mho, Determination of Li^+ diffusion coefficients in the $Li_xV_2O_5$ (x = 0-1) nanocrystals of composite film cathodes, Anal. Sci. 29 (2013) 1083–1088, http://dx.doi.org/10.2116/analsci.29.1083.
[36] E. Potiron, A. Le Gal La Salle, A. Verbaere, Y. Piffard, D. Guyomard, Electrochemically synthesized vanadium oxides as lithium insertion hosts, Electrochim. Acta 45 (1999) 197–214, http://dx.doi.org/10.1016/S0013-4686(99)00204-2.
[37] F. Lantelme, A. Mantoux, H. Groult, D. Lincot, Electrochemical study of phase transition processes in lithium insertion in V_2O_5 electrodes, J. Electrochem. Soc. 150 (2003) A1202–A1208, http://dx.doi.org/10.1149/1.1595658.
[38] S.K. Soni, B.W. Sheldon, X. Xiao, a.F. Bower, M.W. Verbrugge, Diffusion mediated lithiation stresses in Si thin film electrodes, J. Electrochem. Soc. 159 (2012) A1520–A1527, http://dx.doi.org/10.1149/2.009209jes.
[39] K. Zhao, M. Pharr, J.J. Vlassak, Z. Suo, Fracture of electrodes in lithium-ion batteries caused by fast charging, J. Appl. Phys. 108 (2010) 73517, http://dx.doi.org/10.1063/1.3492617.
[40] X. Zhang, W. Shyy, A.M. Sastry, Numerical simulation of intercalation-induced stress in Li-Ion battery electrode particles, J. Electrochem. Soc. 154 (2007) A910–A916, http://dx.doi.org/10.1149/1.2759840.
[41] R. Baddour-Hadjean, J.P. Pereira-Ramos, C. Navone, M. Smirnov, Raman microspectrometry study of electrochemical lithium intercalation into sputtered crystalline V_2O_5 thin films, Chem. Mater. 20 (2008) 1916–1923, http://dx.doi.org/10.1021/cm702979k.
[42] R. Baddour-Hadjean, C. Navone, J.P. Pereira-Ramos, *In situ* Raman microspectrometry investigation of electrochemical lithium intercalation into sputtered crystalline V_2O_5 thin films, Electrochim. Acta 54 (2009) 6674–6679, http://dx.doi.org/10.1016/j.electacta.2009.06.052.
[43] S.K. Soni, B.W. Sheldon, X. Xiao, A. Tokranov, Thickness effects on the lithiation of amorphous silicon thin films, Scr. Mater. 64 (2011) 307–310, http://dx.doi.org/10.1016/j.scriptamat.2010.10.003.